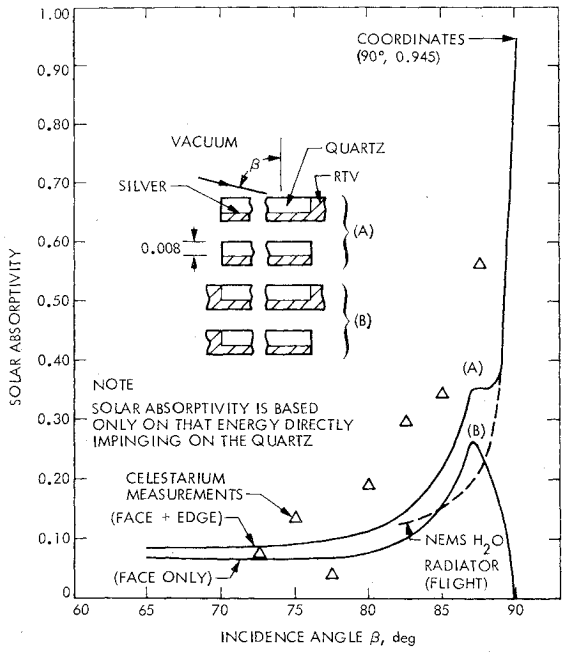

Fig. 3 Solar absorptivity of second surface mirrors at high angles of incidence.

solar absorptivity is based only on the energy impinging on the quartz.

An interesting result observed during these calculations is that for incidence angles greater than 86° (on the face) total capture of the refracted ray occurs if the first and second surfaces of the quartz are out of parallel by less than 0.13°. This is a change of 0.002 in. in 1 in. Since the tolerance on the mirrors is ±0.002 in., the 0.13° criteria is satisfied for a mirror whose thickness decreases uniformly from 0.008 in. at one edge to 0.006 in. at the opposite edge. A mirror meeting this criteria is probably unlikely. However, as the angles of incidence become greater than 86°, the probability of total capture of the refracted ray increases. Mirrors having these geometrical characteristics would exhibit a solar absorptivity higher than that shown in Fig. 3 for angles of incidence between 86° and 89°.

The calculated results explain the hills and valleys of the measurements shown in Fig. 1. Referring to the equations[1] the solar absorptance is greatest at the downward (relative to the incoming ray) mirror edge and decreases rapidly as the opposite edge is approached. The measurement patterns are not ideal because the mirrors are not necessarily in the same plane and one mirror can shade the next at the high incidence angles. Also, measurements indicate that some mirrors bulge at the center as a result of more RTV adhesive at the center than at the corners.

Celestarium

The purpose of the celestarium measurements was to indicate an increase in absorptance and not the magnitude of the absorptance. If it is arbitrarily assumed that the maximum spike (Fig. 1) is representative of an average solar reflectance of 0.925 ($\alpha=0.075$) at $\beta=72.5°$ and the other spikes are assumed proportional to this reflectance, then the results superimposed on Fig. 3 are obtained. The celestarium data supports the calculated trend.

NEMS Radiator

The calculated solar adsorptance for the NEMS H_2O radiator based upon the flight temperatures during a period of constant solar intensity is also shown in Fig. 3. Because of outgassing contamination these results are not truly representative of the solar absorptance of the second surface mirrors. However, like the celestarium measurements, they do indicate the same trend as that calculated by wave theory and does indicate that, despite the contamination, the controlling solar absorptance of the radiator is that of the mirrors.

Conclusions

Test and calculations indicate an increase rather than a decrease in solar absorptance of second surface mirrors at angles of incidence greater than 80°. In practical applications, this effect will be insignificant because, although the solar absorptance is high, the projected area is compensatingly small, resulting in an insignificant increase in the solar or albedo load. However, a spin-stabilized spacecraft can expose second surface mirrors to all angles of incidence. Also, reflected solar energy from a planet or other spacecraft surface could impinge predominantly in the region of high angles of incidence. If a large area is involved, the total load co d be significant. Also, if the spacecraft trajectory is towar he sun, the additional loading would become progress ly larger. Obviously, a concentration of solar energy this high absorptance region could have a disastrous ef ct on a thermal design if overlooked.

More tests are needed to authenticate the calculated results, but to the author's knowledge, none are currently planned. It is recommended that, until better solar absorptivity data is available, the calculated results be used for design purposes.

References

[1] Stultz, J. W., "Solar Absorptance of Second Surface Mirrors for High Angles of Incidence," AIAA Paper 74-670, Boston, Mass., 1974.

[2] Lovin, J. K. and Spradley, L. W., "Lockheed Orbital Heat Rate Package (LOHARP)," HREC-0414-3, April 1970, Lockheed Missiles and Space Company, Sunnyvale, Calif.

Launch Vehicle Trajectory Optimization including Rotational Dynamics

V. Adimurthy*
Space Science and Technology Centre, Trivandrum, India

Nomenclature

$C_{N\alpha}$ = pitching moment coefficient
D = drag force
F_c = control force
g = acceleration due to gravity
g_0 = sea-level acceleration due to gravity
h = altitude
I = vehicle attitude angle
J = performance index
L = lift force
M_c = control moment
MI = moment of inertia about pitch axis
Re = radius of earth
S = reference area
T = thrust
v = magnitude of inertial velocity
v_R = relative velocity

Received June 2, 1975; revision received September 24, 1975. The author wishes to thank M. C. Mathur and C.L. Amba Rao for their encouragement and advice. The programing assistance of K.V. Joy is sincerely appreciated.

Index categories: LV/M Dynamics and Control; LV/M Trajectories.

*Scientist, Aerodynamics Division.

W = weight
ω = weightage for the penalty function
χ = angle between relative velocity and inertial flight path
X_{CG} = distance of center of gravity from vehicle base
X_{cp} = distance of center of pressure from vehicle base
α = angle between vehicle axis and inertial flight path
β = inertial flight path angle measured from local horizontal
θ = range angle
ρ = atmospheric density

Introduction

IN conventional nonlifting type of launch vehicles, trajectory optimization is resorted to after clearing the high dynamic pressure regimes of the dense atmosphere. As the steering during the atmospheric flight is constrained by factors other than optimizing performance, such as aerodynamic loading, essentially a near-zero-angle-of-attack trajectory is recommended.[1] In those portions of the trajectory which are determined by optimization theory (calculus of variations or parametric optimization), it is necessary to choose proper control variables. It is customary to use either the attitude angles[2] or their rates.[3] The attitude rates (pitch and yaw rates) have the advantage of ensuring continuous attitude angles without imposing an extra condition. However, even when the attitude rates are used as the control variable, the moment equations of motion are essentially neglected. This results in a discontinuity in the attitude rate at the corner points. This may not be a serious limitation for vehicles having sufficiently high control-force availability and small control delays. Otherwise, it is useful to include the rotational dynamics while doing the trajectory optimization analysis. Because of the additional differential equation, the discontinuity in the pitch rates is removed and the rotational effects are included. In such a formulation, the pitching moment can be taken as the control variable, as is done here.

In the present Note, only the pitch plane motion is analyzed. In this plane, the vehicle has three degrees of freedom. The vehicle used for numerical computations is a four-stage launch vehicle capable of placing moderate payloads in about 400 km circular orbits. It is assumed that the required aerodynamic, thrust and mass data are known. The control force is of proportional type acting at the nozzle end and normal to the vehicle. The optimization itself is done on the basis of Pontryagin's maximum principle using direct search methods with the conjugate gradient algorithm.[4] The results are compared with earlier results[5] using two degrees of freedom analysis with pitching rate as the control variable. Also presented for comparison are the results for parametric optimization, where constant pitch rates are sought in fixed time blocks.

Mathematical Formulation

The vehicle dynamics is assumed to be governed by the following pitch-plane equations:

$$\frac{dv}{dt} = g_0 \frac{T\cos\alpha - F_c\sin\alpha - D\cos\chi - L\sin\chi}{W} - g\sin\beta \quad (1)$$

$$\frac{d\beta}{dt} = \left[\frac{v}{Re+h} - \frac{g}{v}\right]\cos\beta + \frac{g_0}{v} \frac{T\sin\alpha + F_c\cos\alpha - D\sin\chi + L\cos\chi}{W} \quad (2)$$

$$\frac{dh}{dt} = v\sin\beta \quad (3)$$

$$\frac{d\theta}{dt} = \frac{v\cos\beta}{Re+h} \quad (4)$$

$$\frac{dI}{dt} = \dot{I} \quad (5)$$

$$\frac{d\dot{I}}{dt} = \frac{SC_{N\alpha}(X_{CG}-X_{cp})\rho v_R^2(\alpha - X)}{2MI} + \frac{M_c}{MI} \quad (6)$$

where

$$g = g_0 Re^2/(Re+h)^2 \quad (7)$$

$$I = \pi/2 + \theta - \alpha - \beta \quad (8)$$

Figure 1 describes the various angles involved. In the examples given here, the performance index to be minimized is defined as

$$J = -v_f + \omega(h_f - h_p)^2 \quad (9)$$

where f denotes the final value and h_p is the prescribed altitude of orbit injection. The optimization is performed by an iterative, conjugate gradient search method, after solving in each iteration the costate equations of the above system backwards with appropriate transversality conditions.

Discussion of the Results

The first stage of the vehicle is governed by a pre-set angle-of-attack program, culminating in a gravity turn. These end values form the initial values for the trajectory optimization. In a typical case, the values are as follows: $v = 1.360$ km/sec, $h = 15.798$ km, $\beta = 37.70°$, $\theta = 0.13°$, $I = 39.12°$, and $\dot{I} = 0.40$ deg/sec. These values are obtained from a six degrees of freedom simulation of the first stage.

The results are presented in Figs. 2 and 3. While making the comparisons, care has been taken that the simulations are compatible. In all the cases, the conjugate gradient method is used for optimization, with the same one-dimensional search technique. The weightage ω in the penalty function is the same and is increased by the same factor from iteration to iteration. In Fig. 2, the optimal pitch-rate histories are drawn for the cases of the pitch rate (Ref. 5) and the pitching moment (present formulation) as control variables. Pitch-rate control variable gives an initial discontinuity in the pitch rate. It gives a value of 0.52 deg/sec against the prescribed value of 0.40 deg/sec. The detailed profile also differs significantly from the present results. For comparison we have solved the present formulation with a changed initial condition of $\dot{I}(0) = 0.52$ deg/sec (thus intentionally allowing a discontinuity from first stage burnout value). The pitch-rate control variable curve is nearer to this new profile, but the details are still different, showing the cumulative rotational effects. In Fig. 3, similar

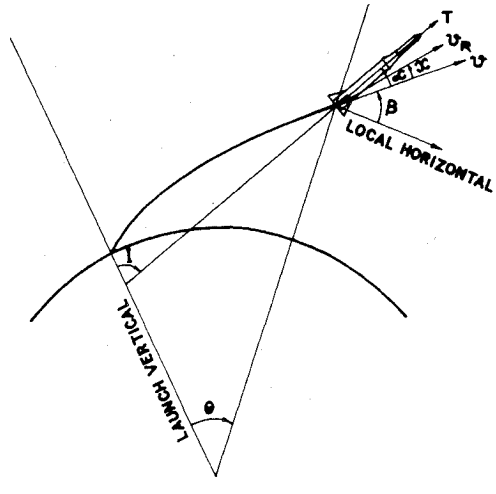

Fig. 1 Schematic representation of angles.

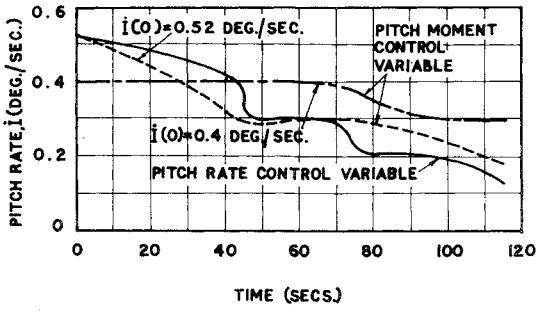

Fig. 2 Comparison of pitch-rate history with pitching moment and pitch rate as control variables.

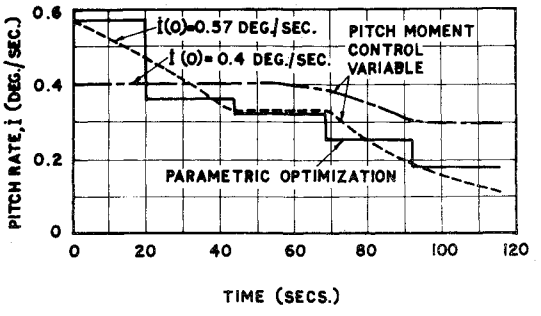

Fig. 3 Comparison of pitch-rate history with pitching moment and discretized pitch-rate as control variables.

comparisons are made with parametric optimization with discretized pitch-rates as parameters. Here, $\dot{i}$ (0) comes to be 0.57 deg/sec, instead of the given value of 0.4 deg/sec. This figure also shows that the pitch-rate control variable results differ significantly from the results of the present analysis.

The final altitude in all the above cases is the same (400 km) to an accuracy of 0.01 km. The injection is horizontal. The velocity with the discretized pitch-rate concept is the highest and is 7.812 km/sec. This velocity is decreased to 7.808 km/sec when the continuous pitch-rate control variable smoothes out the discretized profile. However, in both the cases we have a discontinuity at the initial time. When this is removed by using pitching moment as the control variable, the final velocity is 7.783 km/sec, showing a reduction of about 30 m/sec. These results show that the inclusion of the rotational dynamics can be important in the study of trajectory optimization. This formulation removes various kinds of discontinuities present in the other formulations, and shows a reduction in the final performance. An ideal control system is used in this formulation. This can be modified to include the control system delays and other realistic factors.

References

[1] Spurlock, O.F. and Zarett, H., "Optimal Launch Trajectories for the ATS-E Mission," *Journal of Spacecraft and Rockets,* Vol. 8, Dec. 1971, pp. 1202-1208.

[2] Kelly, H.J., Uzzell, B.R. and McKay, S.S., "Rocket Trajectory Optimization by a Second-Order Numerical Technique," *AIAA Journal,* Vol. 7, May 1969, pp. 879-883.

[3] Rosenbaum, R., "A Combination of Numerical-Analytical Approach to Ascent Trajectory Optimization," AAS Science and Technology Series, Vol. 11, American Astronautical Society, Washington, D.C., 1967, pp. 243-262.

[4] Leondes, C.T. and Wu, C.A., "The Conjugate Gradient Method and its Application to Aerospace Vehicle Guidance and Control-I. Basic Results in Conjugate Gradient Method," *Astronautica Acta,* Vol. 17, Dec. 1972, pp. 871-880.

[5] Adimurthy, V. and Joy, K.V., "Trajectory Optimization of SLV-3" SSTC-ARD-TR-71-75, Jan. 1975, Space Science and Technology Centre, Trivandrum, India.

Shock Interference Peak Heating Measurements using Phase Change Coatings

J. Wayne Keyes*
NASA Langley Research Center, Hampton, Va.

Nomenclature

h	= heat transfer coefficient
M	= Mach number
n	= exponent, Eq. (1)
p	= pressure
PC	= phase change coating data, Fig. 3.
R	= Reynolds number
t	= time
T	= temperature
TC	= thermocouple data, Fig. 3
θ_{SL}	= shear-layer angle relative to local surface inclination

Subscripts

p	= peak
pc	= phase change
s	= stagnation
t	= total
w	= wall
$1,2,3,$ $4,5$	= regions of flowfield, Fig. 1

Introduction

THE phase change coating technique[1] has been used to obtain peak heating measurements in shock interference flow regions with high surface shear and heating.[2-4] This technique provides heat transfer coefficients which are determined by measuring the time for a point on the surface to reach the phase change temperature of the thin fusible coating. These values of time and temperature are then used with the solution to the transient one-dimensional heat conduction equation by assuming a step increase in heat input to ascertain the heat transfer coefficient. Motion picture photography is used to record the phase change pattern, and a precision clock is used to record the time required for the phase change to occur.

The purpose of this Note is to discuss some of the problems encountered in applying the phase change coating technique and to present new shock interference peak heating data which illustrates these problems. A 5.08-cm diameter hemisphere-cylinder made of silica based epoxy was tested at Mach 6 for freestream Reynolds numbers of 3.3 to 25.6 million per meter. Flat plate shock generator angles varied from 5° to 25°. A sketch of the shock interference pattern is shown in Fig. 1. This shock pattern consists of a plane shock intersecting the curved bow shock of the hemisphere thus creating a shear layer (type III interaction, Ref. 3) which attaches to or interacts with the hemisphere boundary layer causing high local pressure and heat transfer. Heating data obtained on a 5.08-cm diameter thin wall stainless steel hemispherical model instrumented with thermocouples every 5 deg on the vertical center line is also presented for the purpose of comparing the phase change technique with the thermocouple-calorimeter method.

Received July 21, 1975; revision received September 23, 1975.

Index categories: Boundary Layers and Convective Heat Transfer-Turbulent; Jets Wakes, and Viscid-Inviscid Flow Interactions; Supersonic and Hypersonic Flow.

*Aerospace Engineer, Applied Fluid Mechanics Section, High-Speed Aerodynamic Division.